Acta Materialia 201 (2020) 412–424

Contents lists available at ScienceDirect

Acta Materialia

journal homepage: www.elsevier.com/locate/actamat

Enhancement of fatigue resistance by overload-induced deformation twinning in a CoCrFeMnNi high-entropy alloy

Tu-Ngoc Lam[a,b], Soo Yeol Lee[c,*], Nien-Ti Tsou[a], Hung-Sheng Chou[a], Bo-Hong Lai[a], Yao-Jen Chang[d,e], Rui Feng[f], Takuro Kawasaki[g], Stefanus Harjo[g], Peter K. Liaw[f], An-Chou Yeh[d,e], Ming-Jun Li[a], Ren-Fong Cai[h], Sheng-Chuan Lo[h], E-Wen Huang[a,e,*]

[a] *Department of Materials Science and Engineering, National Chiao Tung University, 1001 University Road, Hsinchu 30010, Taiwan*
[b] *Department of Physics, College of Education, Can Tho University, Can Tho City 900000, Vietnam*
[c] *Department of Materials Science and Engineering, Chungnam National University, Daejeon 34134, Republic of Korea*
[d] *Department of Materials Science and Engineering, National Tsing Hua University, Hsinchu 30013, Taiwan*
[e] *High Entropy Materials Center, National Tsing Hua University, Hsinchu 30013, Taiwan*
[f] *Department of Materials Science and Engineering, The University of Tennessee, Knoxville, TN 37996, USA*
[g] *J-PARC Center, Japan Atomic Energy Agency, 2-4 Shirakata, Tokai-mura, Naka-gun, Ibaraki 319-1195, Japan*
[h] *Material and Chemical Research Laboratories, Industrial Technology Research Institute, Hsinchu 31057, Taiwan*

A R T I C L E I N F O

Article history:
Received 27 June 2020
Revised 21 September 2020
Accepted 8 October 2020
Available online 13 October 2020

Keywords:
High-entropy alloy
fatigue-crack growth
overload
deformation twins
neutron diffraction

A B S T R A C T

We examined fatigue-crack-growth behaviors of CoCrFeMnNi high-entropy alloys (HEAs) under as-fatigued and tensile-overloaded conditions using neutron-diffraction measurements coupled with diffraction peak-profile analyses. We applied both high-resolution transmission electron microscopy (HRTEM) and neutron-diffraction strain mapping for the complementary microstructure examinations. Immediately after a single tensile overload, the crack-growth-retardation period was obtained by enhancing the fatigue resistance, as compared to the as-fatigued condition. The combined mechanisms of the overload-induced larger plastic deformation, the enlarged compressive residual stresses and plastic-zone size, the crack-tip blunting ahead of the crack tip, and deformation twinning governed the pronounced macroscopic crack-growth-retardation behavior following the tensile overload. A remarkable fracture surface of highly-periodic serrated features along the crack-propagation direction was found in the crack-growth region immediately after the tensile overload. Moreover, a transition of plastic deformation from planar dislocation slip-dominated to twinning-dominated microstructures in the extended plastic zone was clearly observed at room temperature in the overloaded condition, in accordance with the simulated results by a finite element method (FEM). The above tensile overload-induced simultaneously combined effects in the coarse-grained CoCrFeMnNi shed light on the improvement of fatigue resistance for HEAs applications.

1. Introduction

The emerging high-entropy alloys (HEAs) [1] possessing exceptional strength-ductility combination, superior fracture toughness, and thermal stability [2–9] have widely attracted great interest at various temperatures [10] ranging from cryogenic [11] to high temperatures [12] for many potential applications [4,13,14]. For the practical uses of the HEAs, the endurance to fatigue is the key issue [15,16]. However, compared to the dynamic HEAs research, the investigations of fatigue-crack-growth behavior of HEAs under variable-amplitude loading in HEAs are rarely reported. Therefore, it is imperative to unravel the overload effects on the HEAs, accompanied by the known overload-induced major mechanisms of the crack-closure and crack-tip plasticity in the conventional metallic alloys [17–20].

In this study, we selected the Cantor alloy, CoCrFeMnNi, the most widely-investigated HEA system, which is in a single-phase face-centered-cubic (fcc) crystal structure [21]. Although comprehensive research has been devoted to its excellent mechanical behaviors induced by deformation twins under monotonic loading at cryogenic temperatures in the CoCrFeMnNi HEA [2,21–23], the corresponding research on the crack-propagation behavior under fa-

* Corresponding author.
E-mail addresses: sylee2012@cnu.ac.kr (S.Y. Lee), EwenHUANG@nctu.edu.tw (E.-W. Huang).

https://doi.org/10.1016/j.actamat.2020.10.016

tigue loading of the compact-tension (CT) specimen of the American Society for Testing and Materials (ASTM) Standards is limited. Specifically, Suzuki et al. identified the evolution of planar dislocation slip-driven stress-shielding effects on the fatigue-crack-propagation mechanism of the dog-bone CoCrFeMnNi specimen [24]. Thurston et al. specified the increased fatigue-threshold values at smaller load ratios and lower temperatures, affected by the primary deformation mechanism of dislocation activities coupled with the roughness-induced crack closure in the CrMnFeCoNi HEA [25,26]. Rackwitz et al. have recently indicated the major mechanism of roughness-induced crack closure in governing the increased fatigue-threshold values at lower temperatures and larger grain sizes in the CrCoNi medium-entropy alloy (MEA) [27]. In accompanying with the single-phase CoCrFeMnNi HEA, there have been relatively few preliminary studies on the fatigue behavior of multiphase HEAs. Seifi et al. found favorable fatigue resistance of very high fatigue threshold values at lower load ratios and moderate Paris slopes at higher load ratios in the two-phase as-cast Al-based HEAs [6]. Tang et al. discovered the main contribution of predominant nanotwins during cyclic loading at high stresses with the outstanding fatigue resistance of the two-phase wrought $Al_{0.5}CoCrCuFeNi$ HEA having high purity elements [7]. Numerous efforts from the aforementioned research have been made into a complete understanding of the fatigue-crack-growth behavior under constant cyclic loading. However, the geometries of the aforementioned tested HEA specimens were on the small scale. We are thus intrigued by following questions: (1) what happens to the fatigue-crack-propagation performance if we apply variable-amplitude cyclic loading, particularly much higher tensile overload, with the full-size geometry of the ASTM Standards E647-99 [28], (2) would the applied overload be able to activate deformation twins at room temperature, and (3) if there exist overload effects on cyclic loading-induced twins, what their distribution will be and how large the effective size will be as a function of the distance from the crack tip?

We herein address aforementioned issues by investigating the effects of a single tensile overload on the macroscopic fatigue-crack-growth performance, the residual strain/stress distributions, the plastic-zone size in the vicinity of the fatigue-crack tip, and the corresponding underlying mechanism under constant- and tensile overload-fatigue conditions using the full-size geometry-based single fcc CoCrFeMnNi specimens. Neutron diffraction was utilized to examine the residual stresses in the vicinity of the crack tip in the three-orthogonal [crack growth (LD), crack opening (TD), and through thickness (ND)] directions. The Convolutional Multiple Whole Profile (CMWP) modeling for analyzing the neutron-diffraction profiles, high-resolution transmission electron microscopy (HRTEM) characterization, and finite element analysis were performed to determine the predominant micromechanism governing the fatigue-crack-growth behavior under the above two different fatigue conditions.

2. Experimental details

2.1. Materials

The CoCrFeMnNi alloy was fabricated by vacuum induction melting (VIM) with equal molar compositions of constituent powders whose purities are more than 99.9% (in weight percent). As analyzed by neutron-diffraction patterns, the as-cast CoCrFeMnNi remains the single-phase fcc crystal structure in both the initial state and after plastic deformation. Hence, the influence of the second phase on the fatigue-crack-growth behavior could be excluded in this study [29–31]. Based on our preliminary research, the modulus of the HEA was measured [32].

2.2. Fatigue-crack-growth test

The CT specimens of CoCrFeMnNi with a width of 50.8 mm and a thickness of 6.35 mm were prepared according to the ASTM Standards E647-99 for the fatigue-crack-growth test [28]. The CT specimens were pre-cracked to an initial crack length of 1.27 mm before the fatigue-crack-growth experiment. Fatigue-crack-propagation tests were carried out using a computer-controlled servo-hydraulic Material Testing System (MTS)-810. The fatigue tests were performed, employing a load-range-control mode of a triangular waveform [P_{max} = 7,400 N, P_{min} = 740 N, a load ratio R (P_{min} / P_{max}) = 0.1, and a frequency of 10 Hz, where P_{max} and P_{min} are the maximum and minimum loads, respectively]. The crack-growth length was measured using a crack-opening-displacement (COD) gauge by the compliance technique [33,34]. The stress-intensity-factor (K) was obtained as follows:

$$K = \frac{P(2+\alpha)}{B\sqrt{W}(1-\alpha)^{3/2}}(0.886 + 4.64\alpha - 13.32\alpha^2 + 14.72\alpha^3 - 5.6\alpha^4) \tag{1}$$

where P is the applied load, B is the thickness of the CT specimen, $\alpha = a/W$, a is the total crack length, and W is the width of the CT specimen.

Two kinds of fatigues tests, namely as-fatigued (steady-state) and tensile-overloaded, were performed to compare the fatigue-crack-growth behavior. The as-fatigued sample was conducted under constant-amplitude cyclic loading (P_{max} = 7,400 N and P_{min} = 740 N) while the overloaded specimen was also subjected to the same magnitude of the constant-amplitude cyclic loading with the addition of a single tensile overload (10,360N, 140% of P_{max}) at the crack length of 16 mm, corresponding to the stress-intensity-factor range (ΔK) of 25 MPa$\sqrt{\text{m}}$ ($\Delta K = K_{max} - K_{min}$, K_{max} and K_{min} are the maximum and minimum stress-intensity factors, respectively), followed by the continuously applied constant-amplitude for the fatigue-crack-growth test until fracture.

2.3. Neutron-diffraction measurement

Neutron diffraction, a non-destructive technique, has a capability of great penetration on the order of centimeters and volume-averaged characteristics that enable the concurrent bulk measurements of three-orthogonal directions of strains/stresses in the interior and at the surface of the CT specimen along the through-thickness direction with a spatial resolution on the order of millimeter [35]. Neutron-diffraction experiments were conducted at TAKUMI in Materials and Life Science Experimental Facilities at Japan Proton Accelerator Research Complex (J-PARC), Japan. The loading direction of the CT specimens was 45° relative to the incident neutron beam, coupled with two detector banks located at ±90°, simultaneously recording diffraction patterns in both the loading and transverse directions. The incident beam slits were 1 mm in width and 2 mm in height, and the diffracted beams were collimated by a 5-mm wide slit, resulting in a gauge volume of 10 mm^3.

The region of neutron-strain mapping, depicted in Fig. 1(a), was carried out in the interior and near the surface of the CT specimens. The three-orthogonal residual-strain mapping was performed as a function of the distance from the crack tip along the crack-growth direction (x) at two different locations, namely the mid-thickness (interior) and 1.5 mm above the mid-thickness (near the surface), to examine the through-thickness dependency on the fatigue behavior [36]. The residual-strain components in the three-orthogonal (x, y, and z, corresponding to the crack growth (LD), crack opening (TD), and through thickness (ND), respectively) directions were measured as a function of the distance from the

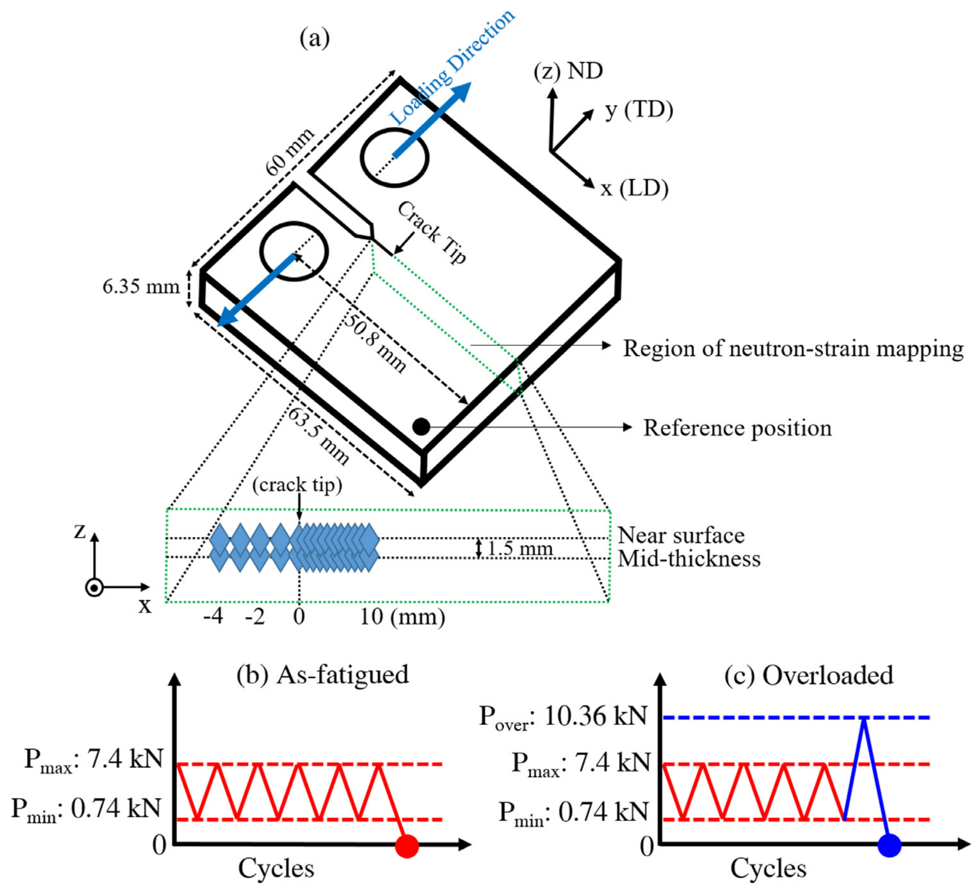

Fig. 1. (a) Schematic illustration of neutron-diffraction-measurement positions around the crack tip. Sample loading conditions for neutron-diffraction measurements in the (b) as-fatigued and (c) overloaded specimens. The red and blue marked circles represent the neutron-measurement positions.

crack tip. The applied load was perpendicular to the crack growth and parallel to the crack-opening direction. The schematic diagram of the spatially-resolved neutron-strain mapping for residual strain/stress profiles as a function of the distance from the crack tip at the two different positions along the through-thickness direction was illustrated in Fig. 1(a).

The lattice-strain dependence of the {311} plane was examined for all strain components (ε_i) along the longitudinal (ε_x), transverse (ε_y), and normal (ε_z) directions because the {311} grain families have less intergranular stresses during plastic deformation in fcc alloys [30,37]. The lattice strain was calculated through the change in the *d*-spacing of the {311} neutron-diffraction peak as a function of the distance from the crack tip along the mid-thickness and near the surface of the CT specimens with respect to the stress-free reference *d*-spacing chosen from the corner of the CT specimens, which is far away from the crack tip. The lattice strain was obtained based on Eq. (2):

$$\varepsilon = (d - d_o)/d_o \tag{2}$$

where d_o is the stress-free reference *d*-spacing, and *d* is the lattice spacing at neutron-measurement positions.

The residual stresses were characterized accordingly in the mid-thickness and near the surface of the CT specimens. The residual-stress components, σ_i, along the three-orthogonal directions (i = x, y, and z, corresponding to the longitudinal, transverse, and normal directions, respectively) were calculated from the three corresponding principal-strain components following the general Hooke's Law Equation.

$$\sigma_i = \frac{E}{1+\upsilon}\left[\varepsilon_i + \frac{\upsilon}{1-2\upsilon}(\varepsilon_x + \varepsilon_y + \varepsilon_z)\right] \tag{3}$$

where E (= 203 GPa) is the Young's modulus and υ (= 0.25) is the Poisson's ratio of the CoCrFeMnNi [38].

The as-fatigued and overloaded samples were prepared for neutron-strain mapping, presented in Figs. 1(b) and (c), respectively. The as-fatigued specimen was subjected to constant-amplitude loading and unloading when the crack length reached 16 mm. The overloaded specimen was prepared immediately after a single tensile overload at the crack length of 16 mm and then unloaded.

The neutron-diffraction profiles were analyzed by the General Structure Analysis System (GSAS) [39] for single-peak fitting and by the CMWP [40] software for resolving the convoluted neutron-diffraction peaks. Since different microstructures are simultaneously governed by distinct diffraction peak profiles such as the peak shift, peak broadening, peak asymmetry, anisotropic peak broadening, and peak shape [41–43], the CMWP analysis was utilized in determining the microstructure-dominated crack-growth behavior, following the previously-used protocol [44–47].

2.4. Microstructural characterization

Fractography analysis was performed by scanning electron microscopy (SEM, JEOL JSM-6700F) operated at 15 keV to identify the correlation between structural features and fatigue properties from the fracture-surface traces during crack propagation. The microstructural features were conducted by high-resolution transmission electron microscopy, JEM-2100F, operated at 200 keV. The HRTEM specimens cut near the crack tip were mechanically ground down to 100 µm, subsequently thinned by the diamond-polishing paper (a diamond-film sheet) and polished with a 0.02 µm non-

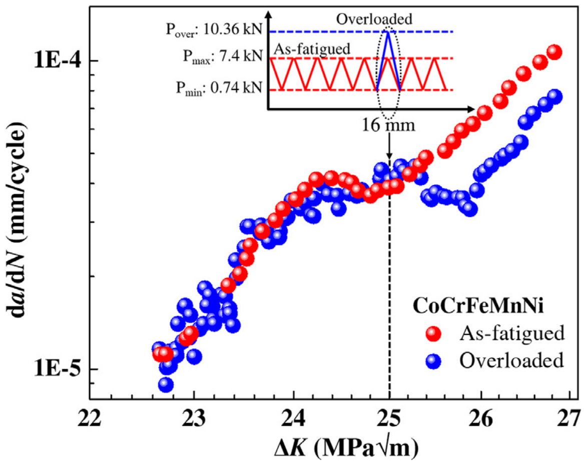

Fig. 2. The crack-growth rate versus stress-intensity-factor range for the as-fatigued and overloaded CoCrFeMnNi samples. The schematic of two different fatigue tests was illustrated in the inset.

crystallizing colloida silica polishing suspension, finally Ar ion-milled in a Gatan Precision Ion Polishing System (PIPS).

2.5. Finite element simulations

Finite element simulation with the ANSYS software [48,49] was implemented to simulate the distribution of the principal stress and shear stress in the vicinity of the crack tip upon unloading at the crack length of 16 mm under constant- and tensile overloaded-fatigue conditions. The simulated CoCrFeMnNi specimens following ASTM Standards E647-99 were set as isotropic elasticity/plasticity, which enabled the occurrence of the large plastic deformation by taking geometric nonlinearity into account [50]. An appropriate mesh refinement around the crack tip is critical for the accurate simulation of the crack-tip field [50]. A refined mesh region with a radius of 5 mm around the crack tip was adopted. The element size of the refined mesh region was 100 nm with the shape of a radial mesh. An ANSYS built-in element type, SOLID185, which is a hexagonal element with six nodes, was used to build the finite element model. Due to the large plastic deformation, the analysis option, “NLGEOM”, in ANSYS is turned on to solve the geometric nonlinearity [50]. The method of the boundary condition was applied, following the previously-used protocol [51].

3. Results

3.1. Fatigue-crack propagation with and without overloading

Fig. 2 presents the fatigue-crack-growth rate (da/dN) as a function of ΔK for two different loading conditions. The crack-growth-rate slopes in the CoCrFeMnNi alloys increased linearly with increasing ΔK in the smaller ΔK region following the Paris law. However, a fairly-invariable range of crack-growth rates was unexpectedly found, which is beneficial to delay the fatigue-crack propagation in the overloaded CoCrFeMnNi. Such an impressive delay phenomenon was also obtained in the previously-reported two-phase as-cast AlCrFeNiCu HEA at $R = 0.1$ [6]. However, further investigation on reasonable factors affecting its fracture resistance needs to be extensively examined. Compared with the as-fatigued sample, the overloaded case unveils a remarkably longer delay range, indicating an obvious crack-growth-retardation period in the ΔK range of 25.2 to 26.8 $MPa\sqrt{m}$ after overloading. The slowest crack-growth rate representing the maximum crack-growth delay was determined at the $\Delta K = 25.9$ $MPa\sqrt{m}$. To compare the fatigue-crack-growth properties and the overload-induced retardation mechanism in the CoCrFeMnNi, we firstly explore the evolution of residual strain and stress profiles around the crack tip.

3.2. Residual strain/stress distribution in the as-fatigued CoCrFeMnNi

To clarify the impact of the stress state on the residual stress along the through-thickness direction, we examined the evolution of the residual strain and stress around the fatigue-crack tip at the mid-thickness and the surface (center + 1.5 mm) positions for the as-fatigued and overloaded cases in the three-orthogonal directions. Fig. 3 presents the residual strain and stress dependence as a function of the distance from the crack tip at the mid-thickness and the surface positions along the three-orthogonal directions in the as-fatigued CoCrFeMnNi specimen.

Similar evolution of the compressive residual strain and stress profiles was observed in the interior and the surface of the as-fatigued specimen. In the LD in Figs. 3a and b, the compressive residual strain/stress regions from −2 to ~5 mm near the crack tip were observed at the mid-thickness, which is slightly larger than the regions from −2 to ~4 mm at the surface. The zone size of the compressive residual strain/stress was wider in front of the crack tip at both the mid-thickness and surface along the LD. A negligible discrepancy of the maximum compressive residual strain/stress near the crack tip was obtained between the two locations in the as-fatigued CoCrFeMnNi.

In the TD of Figs. 3c and d, a slightly-higher maximum compressive residual strain/stress at the crack tip was found at the mid-thickness than at the surface, and the tensile residual strain/stress began to develop in the position of ~4 mm, ahead of the crack tip. Both the mid-thickness and the surface disclosed similar zones of the compressive residual strain/stress distribution from −4 to ~3 mm. The compressive residual strain/stress profiles in the TD exhibited analogous tendencies with those in the LD. However, the maximum compressive residual strain/stress at the crack tip in the TD (Figs. 3c and d) were 1.5 times larger than those in the LD (Figs. 3a and b).

In Figs. 3e and f, there was no obvious difference in the maximum compressive residual strain/stress near the crack tip between the mid-thickness and the surface in the ND. The maximum compressive residual stress in the ND was almost two or three times smaller than that in the LD and TD. The compressive residual stresses were narrowly distributed from the position of 0 to 2 mm in front of the crack tip at both the mid-thickness and the surface in the ND. There was a very small fluctuation of the compressive residual stresses from the position of −4 to 0 mm behind the crack tip in the ND, which was obviously different from a drastic increase of the compressive residual stresses in the crack-wake region in the LD and TD.

Although there exists a variation in the distribution of the compressive residual stresses near the crack tip at the mid-thickness and the surface positions in the three-orthogonal directions, their compressive residual stress profile trends as a function of the distance from the crack tip were almost alike. The results imply that the as-fatigued CoCrFeMnNi does not clearly reveal thickness-dependent effects, which is analogous to the stainless steel [17].

3.3. Comparison of residual-stress distributions with and without overloading

Fig. 4 depicts the residual-stress dependence as a function of the distance from the crack tip at the mid-thickness in the as-fatigued and overloaded CoCrFeMnNi in the three-orthogonal directions. It is noted that the overload point corresponds to the crack-tip position in the overloaded specimen. Both specimens display analogous tendencies of the compressive residual stress pro-

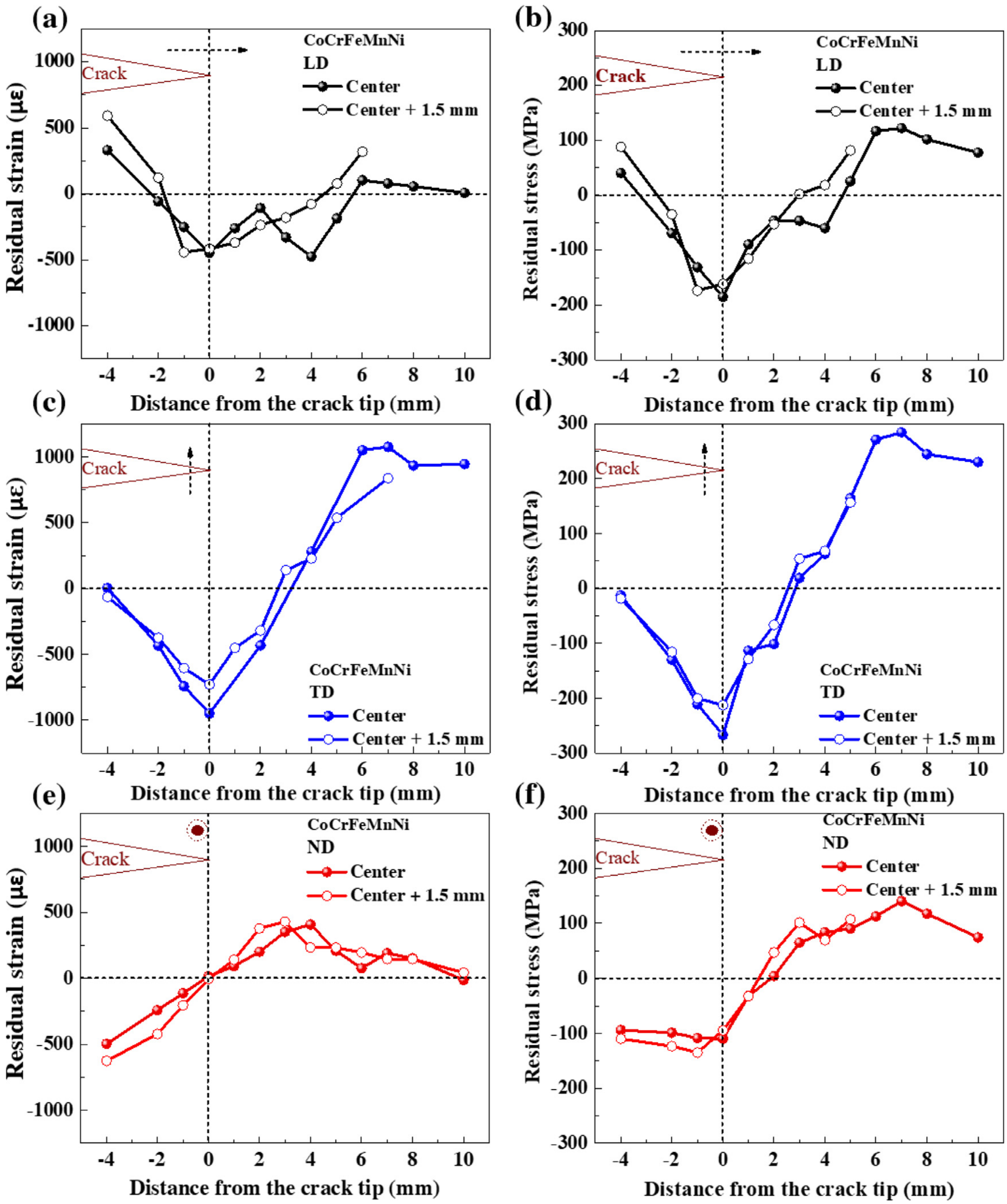

Fig. 3. The residual strain and stress distributions as a function of the distance from the crack tip in the as-fatigued CoCrFeMnNi along the LD in (a) and (b), respectively; those along the TD in (c) and (d), respectively; and those along the ND in (e) and (f), respectively.

files in the three-orthogonal directions. In Fig. 4a, larger compressive residual stresses were distributed in a broader zone size in the overloaded case (a range of −4 to 8 mm) than in the as-fatigued case (a range of −4 to 5 mm) along the LD. The maximum residual stress of −240 MPa at the position of 3 mm in the overloaded specimen was more compressive than that of −185 MPa at the crack tip in the as-fatigued CoCrFeMnNi. A larger zone size of the compressive residual stresses in the overloaded case was also observed along the TD in Fig. 4b. The maximum compressive residual stress decreased slightly at the crack tip after overloading. Along the ND in Fig. 4c, there was a trivial variation of the maximum compressive residual stress near the crack tip between the two specimens. The maximum compressive residual stress in the overloaded CoCrFeMnNi was located ahead of the crack tip in the LD, while it was found behind the crack tip in the TD and ND. Although the distribution of the compressive residual stresses behind the crack tip in the CoCrFeMnNi is more obvious than that in the stainless steel in the identical fatigue conditions [17], no significant discrepancy in the magnitude of the compressive residual stresses in the crack-wake region was found between the as-fatigued and overloaded CoCrFeMnNi. It can be evidently seen from Fig. 4 that the tensile overload results in both the greater zone size and magnitude of the compressive residual stresses ahead of the fatigue-crack tip in all the three-orthogonal directions. The tensile overload-induced larger plastic deformation coupled with the resulting compressive residual stresses ahead of the crack tip are

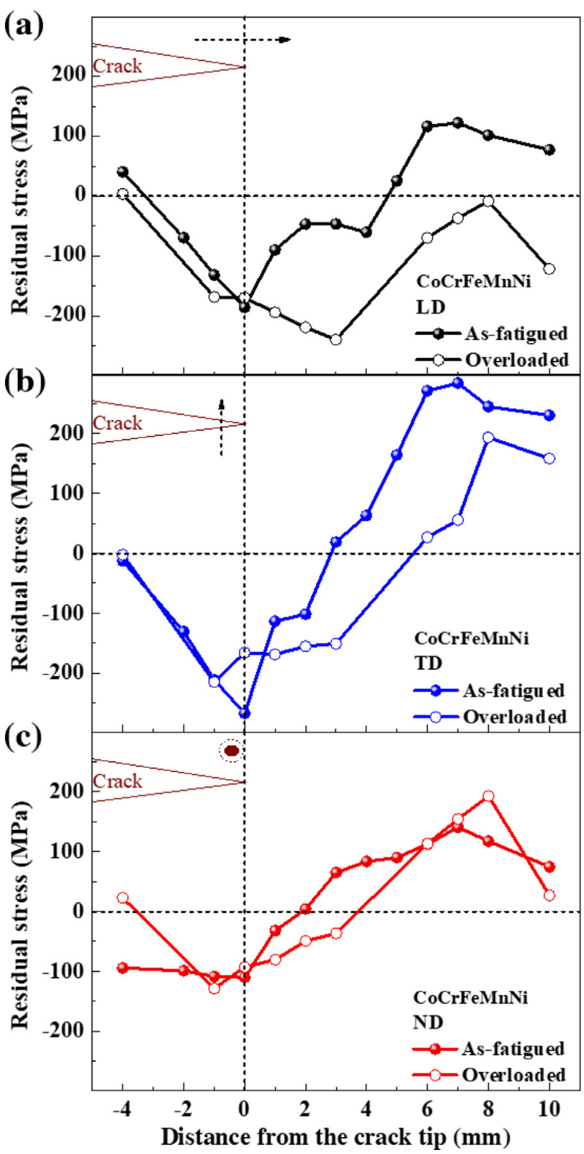

Fig. 4. The residual-stress distribution as a function of the distance from the crack tip at the mid-thickness in the as-fatigued and overloaded CoCrFeMnNi along the (a) LD, (b) TD, and (c) ND.

the major reasons contributing to the crack-growth retardation in the CoCrFeMnNi HEA. The evolution of the residual-compressive stresses in the crack-wake region in the as-fatigued CoCrFeMnNi exhibits a similar propensity with that in the as-fatigued and overloaded stainless steel [17]. On the contrary, the overloaded CoCrFeMnNi reveals a noticeable difference, compared with the as-fatigued CoCrFeMnNi at the crack tip. The residual-compressive stresses in the three-orthogonal directions in the overloaded CoCrFeMnNi were slightly relaxed at the crack tip, while those in the as-fatigued CoCrFeMnNi continued increasing and reached the maximum magnitude at the crack tip. It can be suggested that besides the plasticity ahead of the crack tip, there should have other reasonable factors involving the overload-induced substantial delay of the crack-propagation rate in the CoCrFeMnNi alloy.

3.4. Estimation of the plastic-zone size with and without overloading

Due to the larger plastic deformation following a single tensile overload, the estimation of the plastic-zone size is crucial for a better understanding of the overload-induced retardation mechanism in the CoCrFeMnNi. The plastic-zone sizes in the as-fatigued [Ry(c)] and overloaded [Ry(o)] conditions were defined by the following Irwin's estimations [52] in Eq. (4) and (5), respectively.

$$R_{y(c)} = \frac{1}{\beta\pi}\left(\frac{K_{max}}{\sigma_y}\right)^2 \tag{4}$$

$$R_{y(o)} = \frac{1}{\beta\pi}\left(\frac{K_o}{\sigma_y}\right)^2 \tag{5}$$

where $\beta = 1$ or 3 under plane-stress or plane-strain conditions, respectively. σ_y is the yield strength (203 MPa) of CoCrFeMnNi. K_{max} and K_o are the stress-intensity factors at the maximum load in the steady amplitude and at the overload point, respectively.

Since the thickness of the CT specimen of CoCrFeMnNi is 6.35 mm and there is no significant difference in the residual-stress distribution between the mid-thickness and the surface, the CoCrFeMnNi is assumed to be experiencing the stress state of $\beta = 1$. It was found that the estimated plastic-zone size in the overloaded (7.9 mm) sample was almost twice greater than that in the as-fatigued CoCrFeMnNi (4.0 mm). Since the crack has to move out of the plastic zone to remain the steady-crack-growth stage, the overload-induced larger plastic-zone size contributes to the retardation of the crack-propagation process [53,54].

The shape of the fatigue-crack tip before and after the tensile overload was examined by optical microscopy (OM), shown in Fig. S1 of the Supplementary Information (SI). The crack-tip blunting was evidently observed immediately after both as-fatigued and tensile overload. Therefore, the simultaneous contributions of the overload-induced plasticity ahead of the crack tip with the extended plastic-zone size and crack-tip blunting are closely related to the retardation of the crack growth in the CoCrFeMnNi HEA.

3.5. Fatigue fractography

Fig. 5(a) presents the macroscopic micrograph of the fatigue-fracture surface near the crack tip under a constant-fatigue condition in which the fracture surface becomes rougher when the crack propagates into higher growth rates. The SEM fractographs in Figs. 5(b)-(d) revealed that the fracture surface in the crack-propagation region was characterized by fatigue striations, cleavages, tear ridges, voids, dimples together with microcracks. The fracture feature was covered by voids and dimples ascribed to the ductile fracture mechanism with an increasing ΔK, shown in Fig. 5(e).

The macroscopic fracture surface near the crack tip under the tensile overloaded-fatigue condition was presented using SEM characterization in Fig. 6(a). During the crack-propagation region immediately after the single tensile overload, a striking fracture surface of highly-periodic serrated features along the crack-propagation direction was visible in the red marked region in Fig. 6(a) and enlarged in Fig. 6(b). In conjunction with the predominant serrated features, the cleavages, tear ridges, voids, and dimples were observed in Figs. 6(c-d). Such typical fatigue characteristics of well-aligned periodic serrations might be related to a transition from planar-slip dislocation activities to deformation twinning as the prominent mechanism derived from a much higher local stress distribution at the crack tip, and would retard the crack growth immediately following a single tensile overload. The fracture surface at higher growth rates was different from that of the applied overload region, with the major features of cleavages, voids, and dimples as obtained in Figs. 6(e-f).

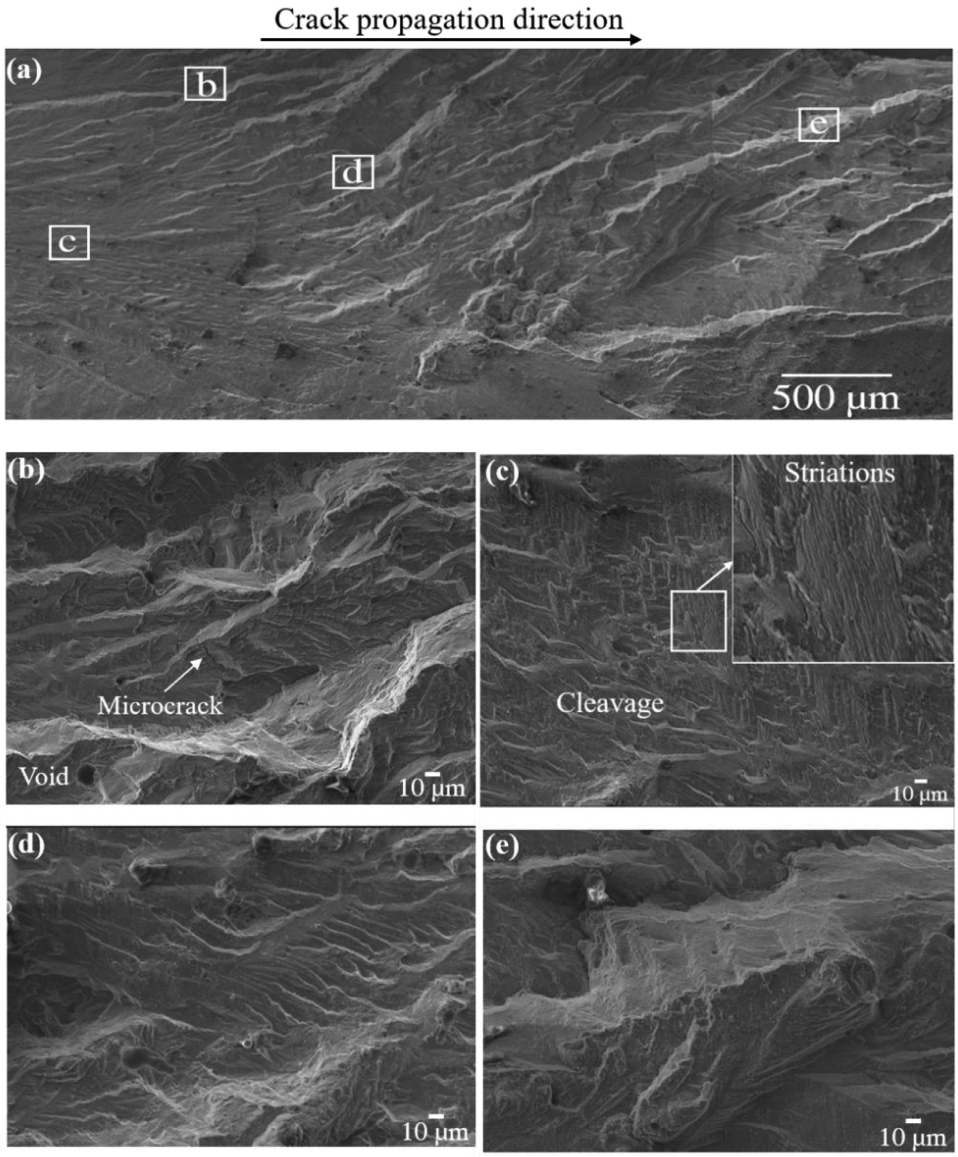

Fig. 5. (a) SEM micrographs of the macroscopic fracture surface under the as-fatigued condition. (b-e) are the magnified images of the corresponding squares in (a).

3.6. Twinning-dominated microstructures of the overload-induced plastic zone

The microstructures of the plastic zone ahead of the crack tip are governed by the stacking fault energy of the material [55,56]. The Cantor CoCrFeMnNi alloy is known to possess the low stacking-fault energy for favorably generating a high degree of stacking faults and deformation twins during loading [57,58], specifically in tension [59]. It has been reported on the deformation-twinning-dominated mechanism of the coarse grains, which strongly influences the mechanical properties as well as the fatigue-crack-growth behavior in the HEAs [22,56,60]. To understand the dominated microstructures within the zone of plastic deformation with/without overloading, we employed CMWP to identify the distribution of dislocation density, formation probability of twins, extrinsic and intrinsic stacking faults [42] as a function of the distance from the crack tip in the as-fatigued and overloaded CoCrFeMnNi, as presented in Fig. 7. The distribution of dislocation density within the corresponding plastic zone was broader in the overloaded sample than in the as-fatigued one due to the overload-induced larger plastic-zone size ahead of the fatigue crack tip (Figs. 7a-c). During the crack-propagation process, the dislocations were generated near the crack tip with higher densities, followed by a gradual decrease towards the end of the plastic zone in both the as-fatigued and overloaded samples. However, much greater density of dislocations was produced after the tensile overload due to the overload-induced larger plastic deformation.

The tensile overload induces a moderately-higher probability of extrinsic (Figs. 7d-f) and intrinsic (Figs. 7g-i) stacking faults in all the three-orthogonal directions. However, intrinsic rather than extrinsic stacking faults were slightly preferentially produced in both the as-fatigued and overloaded CoCrFeMnNi. It is utterly striking that the overload greatly enhances both the density and distribution zone of the twins near the crack tip in all the three-orthogonal directions (Figs. 7j-l). Meanwhile, the results of the as-fatigued specimen show that the cyclically-induced twins are less than those of the tension [59].

The maximum twin probability of approximately 0.6% in the as-fatigued and that of approximately 0.95% in the overloaded CoCrFeMnNi were distributed in the position of 0~2 mm ahead of the crack tip. It is interesting to note that the dislocation density, twin, extrinsic and intrinsic stacking faults distributions correlate well

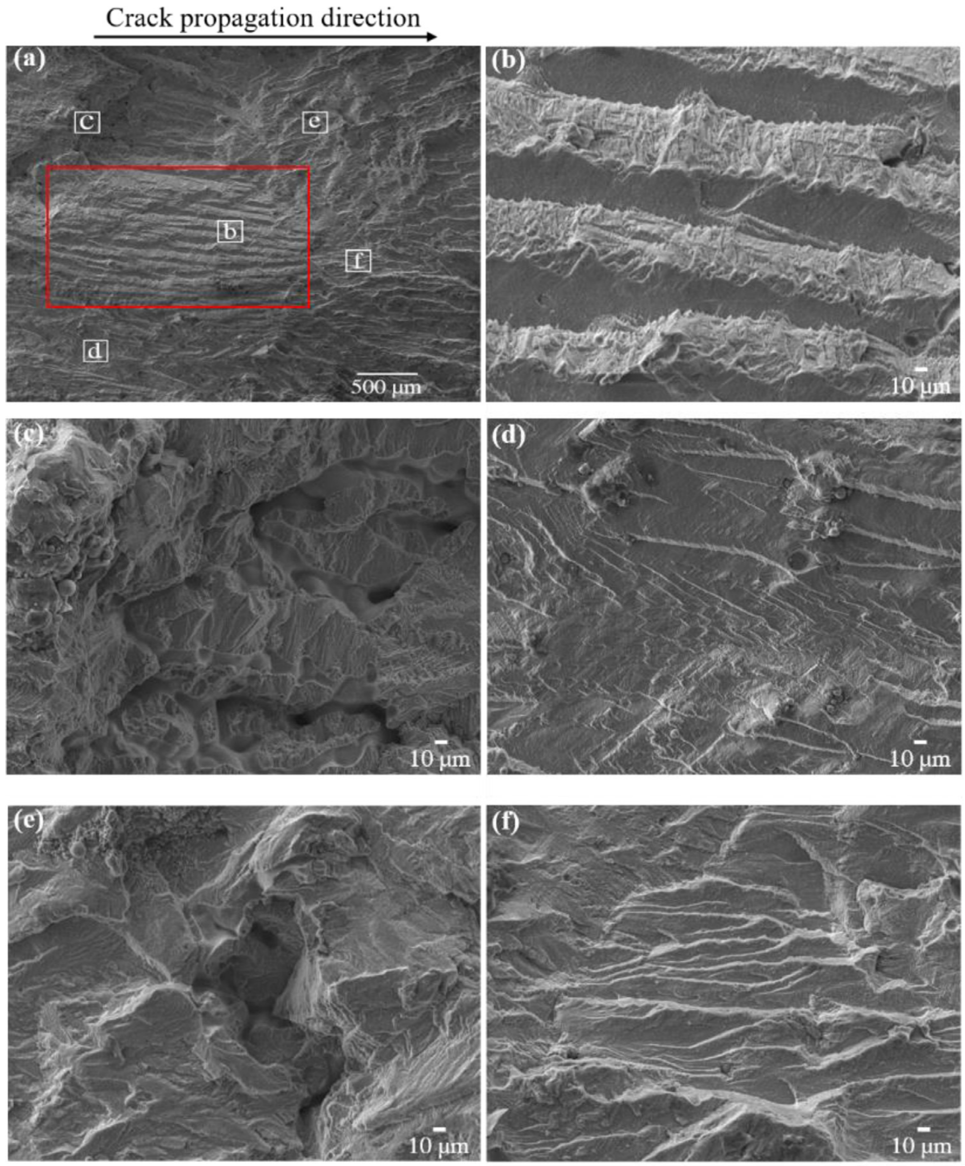

Fig. 6. (a) SEM micrographs of the macroscopic fracture surface under the tensile overloaded-fatigue condition. (b-f) are the magnified images of the corresponding squares in (a).

with the corresponding compressive residual stress distribution and plastic zone. The salient findings in greater densities of dislocation, higher probabilities of twins, extrinsic and intrinsic stacking faults within the extended plastic zone with overloading are believed to improve the fracture toughness in resisting the crack propagation [61,62]. Associated with a higher concentration of the crack-tip stress, the generation of twinning structures is possibly activated near the crack tip. A much greater degree of deformation twins rather than extrinsic and intrinsic stacking faults in the overloaded condition is expected to be observed by HRTEM.

To elucidate the crack-tip behavior governed by dominated microstructures of dislocation-slip activities or twinning structures, HRTEM characterization was performed near the fatigue-crack tip in the as-fatigued and overloaded CoCrFeMnNi samples shown in Fig. 8. Without the overload in Fig. 8a, the presence of the planar dislocation slip as the major mechanism governs the fatigue-crack deformation near the crack tip, which is in reasonable agreement with the prior observation [25]. Meanwhile, a salient formation of twinning structures was evidently visible with selected area electron diffraction (SAED) patterns from the twin and matrix, as demonstrated in Fig. 8b, implying twinning-driven work hardening as the outstanding deformation mechanism near the crack tip in the overloaded specimen. The overload-induced larger plasticity produced sufficiently enough stresses to exceed the critical resolved shear stress for the onset of twinning and triggered the generation of deformation twins near the crack tip even at room temperature, as discussed in the following section.

3.7. Stress distribution around the crack tip simulated by the finite element method (FEM)

In order to examine the magnitude and distribution of the principal and shear stresses in the vicinity of the fatigue-crack tip, which governs the crack-tip deformation behavior, finite element simulations were implemented under constant- and tensile overloaded-fatigue conditions. The stresses were maintained within the zone of plastic deformation upon unloading. Fig. 9(a) illustrates the schematic diagram of the principal and shear stresses distribution from −5 to 5 mm around the crack tip upon unloading with/without the applied tensile overload at the crack length of 16

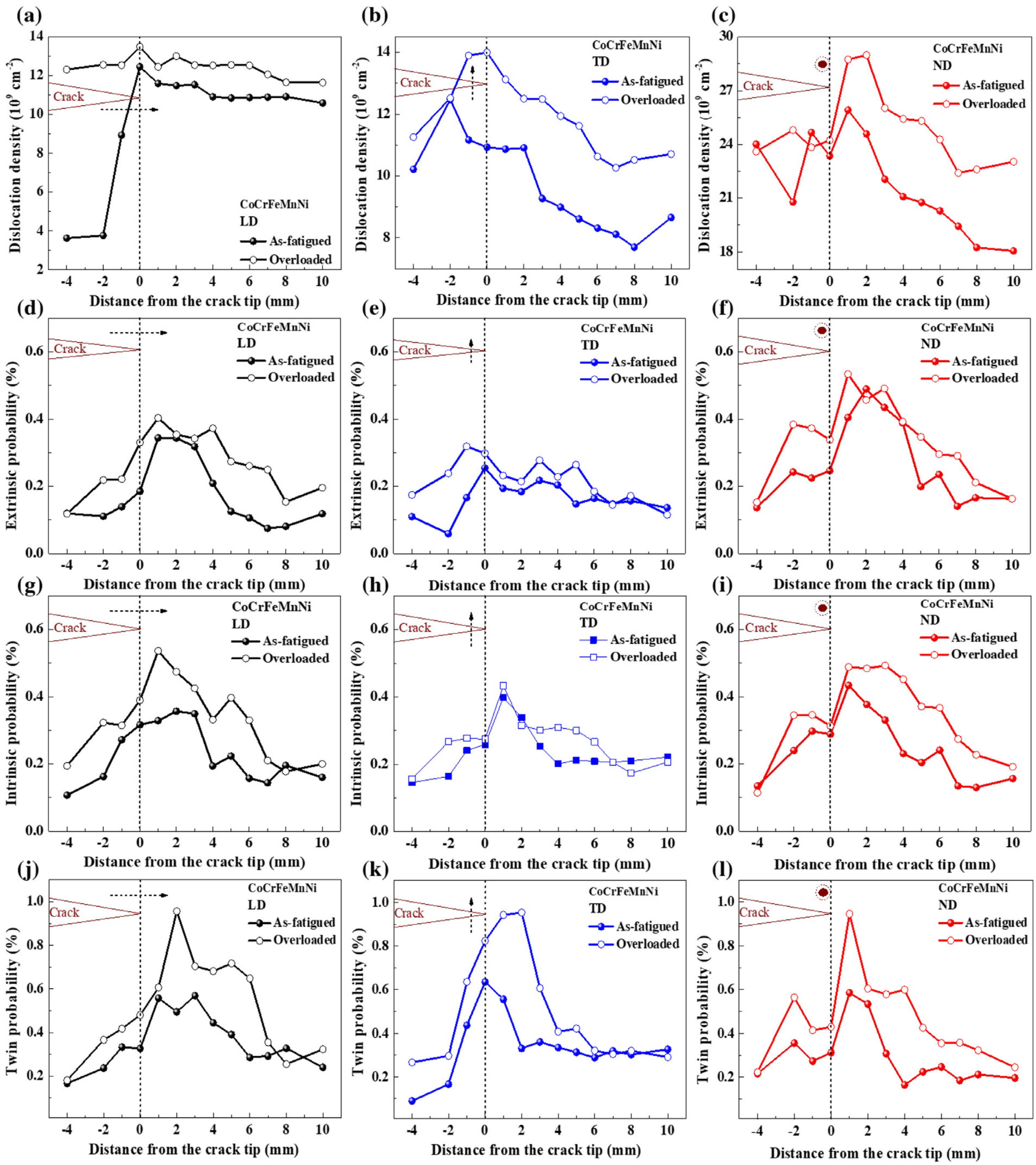

Fig. 7. Dislocation-density distribution in the (a) LD, (b), TD, and (c) ND; Extrinsic stacking-fault probability in the (d) LD, (e), TD, and (f) ND; Intrinsic stacking-fault probability in the (g) LD, (h), TD, and (i) ND; Twin probability in the (j) LD, (k) TD, and (l) ND as a function of the distance from the crack tip in the as-fatigued and overloaded CoCrFeMnNi.

mm with an enlarged mesh-refining region shown in Fig. 9(b). The principal stresses gradients ahead of the crack tip with the maximum values found at the fatigue-crack tip were 658 and 835 MPa in the as-fatigued [Fig. 9(c)] and overloaded [Fig. 9(d)]) specimens, respectively. Moreover, the shear stress homogenously distributed from −1 to 5 mm with the maximum value of 179 MPa in the as-fatigued condition [Fig. 9(e)], which was much lower than that of 281 MPa at the crack tip in the overloaded one [Fig. 9(f)]. As seen in the contour plots in Figs. 9(c)-(f), the maximum principal and shear stresses near the crack tip immediately after a single tensile overload were much greater than those in the as-fatigued specimen, and they exceeded the critical twinning stress of 720 MPa and critical resolved shear stress for twinning formation of 235 MPa in the CrMnFeCoNi HEA [63]. Such the twinning-affected crack-tip behavior in the overloaded specimen at room temperature was demonstrated both in the simulated results by FEM and in the experimental observation of twinning structures by TEM.

4. Discussion

We summarized the fatigue-crack-growth results of the as-cast CoCrFeMnNi at room temperature, together with those of the previously-reported MEA [27], HEAs [6,25], ands austenitic stainless steels [17,25,64] under comparable testing conditions in terms

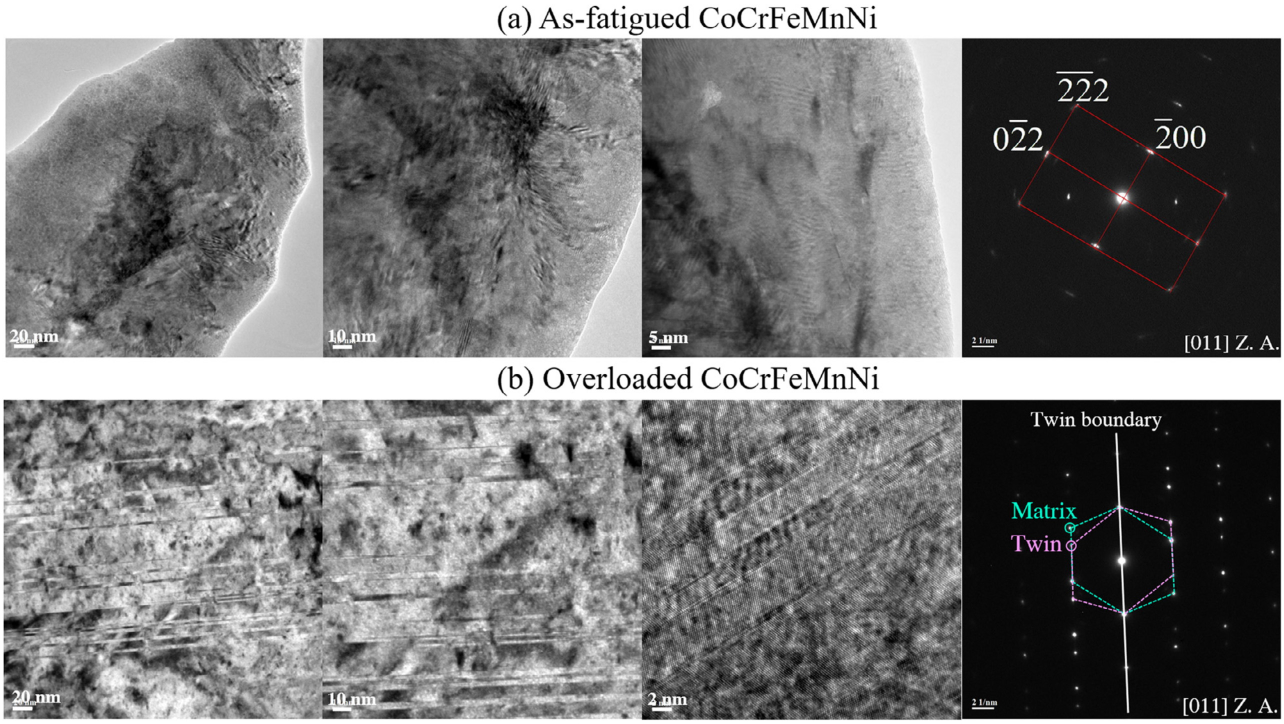

Fig. 8. HRTEM images near the crack tip in the (a) as-fatigued and (b) overloaded CoCrFeMnNi HEA coupled with the corresponding SAED patterns with a zone axis of [011] at room temperature.

Table 1
Summary of fatigue-crack-growth results at room temperature, including previous investigations.

Alloy	R(load ratio)	Frequency (Hz)	Grain size (μm)	Young's modulus(GPa)	CT specimen(width x thickness)(mm)	Paris slope (m)
CoCrFeMnNi	0.1	10	500 – 3,000	203	63.5 x 6.35	7.4
$AlCrFeNi_2Cu$ [6]	0.1	20	-*	-*	20 x 3	3.4
$AlCrFeNi_2Cu$ [6]	0.3	20	-*	-*	20 x 3	6.5
$AlCrFeNi_2Cu$ [6]	0.7	20	-*	-*	20 x 3	14.5
$Al_{0.2}CrFeNiTi_{0.2}$ [6]	0.1	20	-*	-*	20 x 3	4.9
$Al_{0.2}CrFeNiTi_{0.2}$ [6]	0.3	20	-*	-*	20 x 3	5.3
$Al_{0.2}CrFeNiTi_{0.2}$ [6]	0.7	20	-*	-*	20 x 3	25.8
CrMnFeCoNi [25]	0.1	25	7	202	12.5 x 6	3.5
CrCoNi MEA [27]	0.1	25	7	-*	12.4 x 6.1	3.3
CrCoNi MEA [27]	0.1	25	68	-*	12.4 x 6.1	3.9
304 steel [25,64]	0.1	20	-*	200	62.5 x 6	3.8
304L steel [17]	0.1	10	-*	183.5	63.5 x 6.35	-*

* Values were not reported in the corresponding study.

of the grain size, Young's modulus, and CT specimen size, as shown in Table 1.

The as-cast CoCrFeMnNi in the present study exhibited the coarse grains in the size range of 500 – 3,000 μm with microstructural features of dendritic structures, as shown in Fig. S2 of the SI. The small CT specimen size of the fine-grained CrMnFeCoNi HEA exhibits smaller values of threshold ΔK and Paris slope values [25], while the as-cast AlCrFeNi-based HEAs reveal a favorable combination of the highest threshold ΔK values and moderate Paris slopes [6]. The improved fatigue resistance in the as-cast microstructures can be attributed to the increased roughness of fracture surfaces [65]. Our fatigue-crack-growth results show moderate Paris slopes of 7.4, compared with other reported HEAs [6,25] and austenitic stainless steels, which is presumably ascribed to the ASTM standard-based full size geometry of the CT specimens together with the as-cast microstructures of our CoCrFeMnNi HEAs. The large size of CT specimens could remove the excessive plasticity [25]. Furthermore, our neutron-diffraction profiles and TEM results demonstrated that the as-cast CoCrFeMnNi specimens remained the single-phase fcc structure during the two different fatigue tests. It can be suggested that constant-amplitude and variable-amplitude cyclic loadings did not induce phase transition in the as-cast CoCrFeMnNi HEAs since the stress-driven energy was not sufficient to overcome the energy barrier in triggering the phase transformation from the fcc to the hexagonal close-packed (hcp) crystal structure. However, the applied tensile overload revealed the twinning structures-induced work hardening in the CoCrFeMnNi alloy even at room temperature due to high stresses above the critical resolved shear stress of 235 MPa for the activation of twinning near the crack tip, giving rise to the enhanced fatigue resistance for structural applications. In summary, neutron-diffraction mapping coupled with diffraction peak-profile analyses using CMWP, corroborated by HRTEM and simulated FEM results elucidate microscopic insights into the overload effects on the retardation in the crack-growth rate of the CoCrFeMnNi HEA. The reported experimental results here can be useful for the simulation, such as the extended finite element method (XFEM) to determine the stress intensity factors (SIFs), the crack-propagation path, the fatigue lifetime [66], and the twinning-influenced crack propagation [67] of the HEAs.

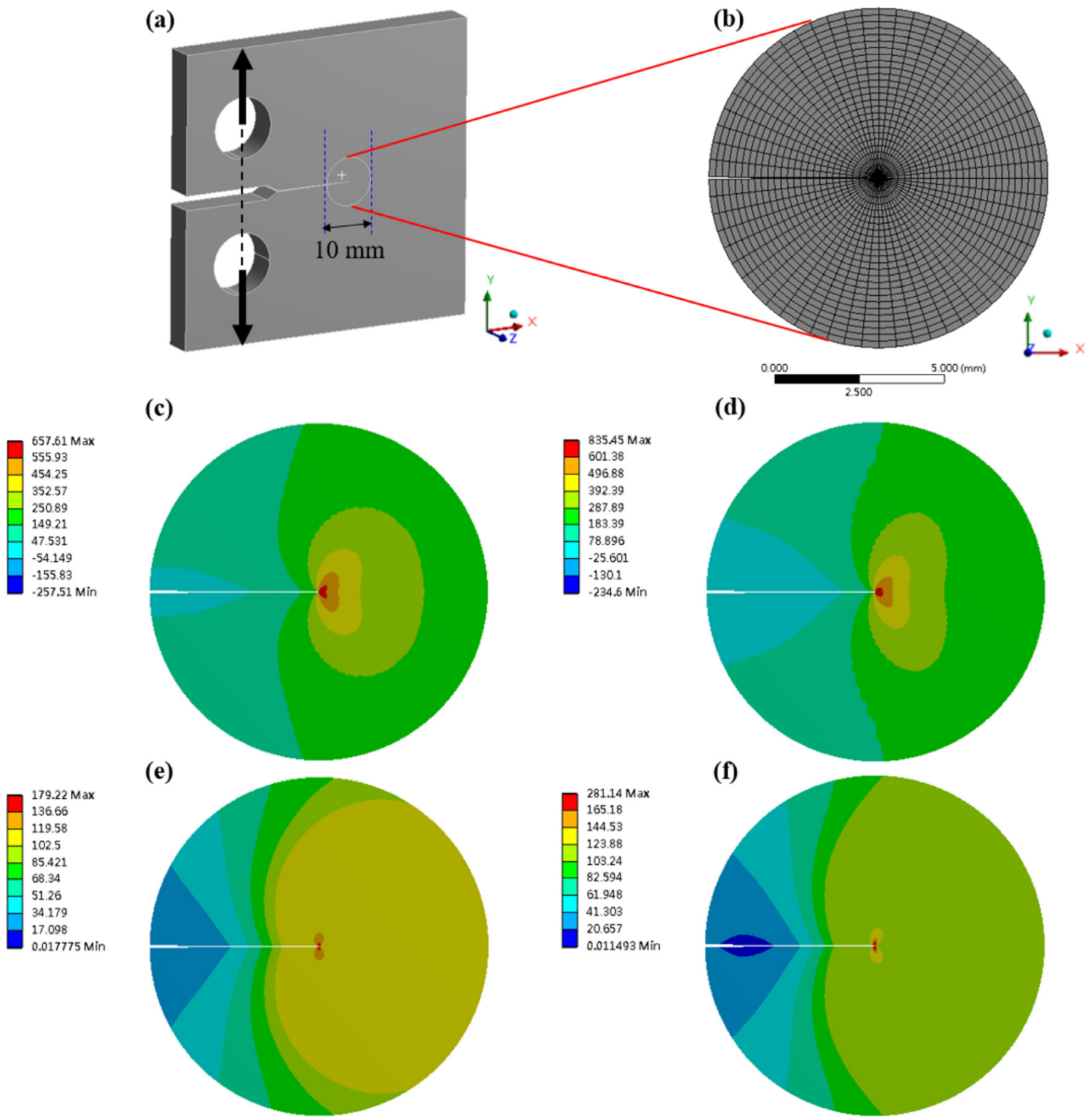

Fig. 9. (a) Schematic diagram of the principal and shear stresses distributions from −5 to 5 mm around the crack tip upon unloading with and without a single tensile overload at the crack length of 16 mm. (b) The enlarged mesh-refining region. The contour plots of the principal stress distribution in the (c) as-fatigued and (d) overloaded specimens; those of the shear stress distribution in the (e) as-fatigued and (f) overloaded specimens.

5. Conclusions

The dislocation slip-dominated microstructures associated with the compressive residual-stress distribution within the plastic zone ahead of the crack tip were the major mechanisms of fatigue-crack growth in the as-fatigued specimen. On the other hand, the crack-tip behavior of twinning-dominated microstructures in the extended plastic zone coupled with the overload-induced larger plasticity ahead of the crack tip and crack-tip blunting governed the crack-growth retardation mechanisms in the single-phase fcc CoCrFeMnNi immediately after the tensile overload. Such combined effects in the overloaded specimen suggest a fatigue-resistant feature for the fatigue-crack growth of the HEAs. The results can be useful for the design of the fatigue-resistant HEAs as well as for fatigue-related simulations and modeling to facilitate their applications.

Declaration of Competing Interest

None.

Acknowledgements

The neutron-diffraction experiments were performed at BL19 in Materials and Life Science Experimental Facility of J-PARC with the proposals of 2016A0322, 2018A0248, and 2018A0248. We acknowledge the Ministry of Science and Technology (MOST), Taiwan, for financial support through Grant No. MOST-108-2739-M-213-001 from the National Synchrotron Radiation Research Center (NSRRC) Neutron Cultivation Program, in providing the trip to J-PARC used in the present work. The authors are grateful to the support of the MOST Programs MOST 108-2221-E-009-131-MY4 and 108-2218-E-007-005. We sincerely appreciate Prof. Tamás Ungár for teaching us the Convolutional Multiple Whole Profile (CMWP) software. We are very grateful to Prof. A.-C. Y. and Dr. Y.-J. C. for fabricating the high quality samples financially supported by the “High Entropy Materials Center” from The Featured Areas Research Center Program within the framework of the Higher Education Sprout Project by the Ministry of Education (MOE) in Taiwan. We really appreciate Prof. P. K. L. and Dr. R.

F. for assisting the crack-growth experiment. We appreciate Mr. Mao-Yuan Luo and Ms. Chia-Yin Ma's assistances for their data analysis. The current work was financially supported by the "Center for the Semiconductor Technology Research" from the Featured Areas Research Center Program within the framework of the Higher Education Sprout Project by the Ministry of Education (MOE) in Taiwan. Also supported in part by the Ministry of Science and Technology, Taiwan, under Grant MOST-109-2634-F-009-029. SYL was supported by the National Research Foundation (NRF) grant funded by the Korean Government (2020M2A2A6A05026873, 2017M2A2A6A05017653, and 2020K1A3A7A09078090). SH also acknowledges the JSPS Kakenhi No. 19H05180. PKL very much appreciates the support of (1) the U.S. Army Research Office Project (W911NF-13-1-0438 and W911NF-19-2-0049) with the program managers, Drs. M. P. Bakas, S. N. Mathaudhu, and D. M. Stepp and (2) the National Science Foundation (DMR-1611180 and 1809640) with the program directors, Drs. J. Yang, G. Shiflet, and D. Farkas.

Supplementary materials

Supplementary material associated with this article can be found, in the online version, at doi:10.1016/j.actamat.2020.10.016.

References

[1] S.-K. Chen, J.-W. Yeh, S.-J. Lin, J.-Y. Gan, T.-S. Chin, T.-T. Shun, C.-H. Tsau, S.-Y. Chang, Nanostructured High-Entropy Alloys with Multiple Principal Elements: Novel Alloy Design Concepts and Outcomes, Advanced Engineering Materials 6 (2004) 299–303.
[2] B. Gludovatz, A. Hohenwarter, D. Catoor, E.H. Chang, E.P. George, R.O. Ritchie, A fracture-resistant high-entropy alloy for cryogenic applications, Science 345 (2014) 1153–1158.
[3] L.J. Santodonato, Y. Zhang, M. Feygenson, C.M. Parish, M.C. Gao, R.J. Weber, J.C. Neuefeind, Z. Tang, P.K. Liaw, Deviation from high-entropy configurations in the atomic distributions of a multi-principal-element alloy, Nat Commun 6 (2015) 5964.
[4] Y. Zhang, T.T. Zuo, Z. Tang, M.C. Gao, K.A. Dahmen, P.K. Liaw, Z.P. Lu, Microstructures and properties of high-entropy alloys, Progress in Materials Science 61 (2014) 1–93.
[5] M.A. Hemphill, T. Yuan, G.Y. Wang, J.W. Yeh, C.W. Tsai, A. Chuang, P.K. Liaw, Fatigue behavior of Al0.5CoCrCuFeNi high entropy alloys, Acta Materialia 60 (16) (2012) 5723–5734.
[6] M. Seifi, D. Li, Z. Yong, P.K. Liaw, J.J. Lewandowski, Fracture Toughness and Fatigue Crack Growth Behavior of As-Cast High-Entropy Alloys, JOM 67 (10) (2015) 2288–2295.
[7] Z. Tang, T. Yuan, C.-W. Tsai, J.-W. Yeh, C.D. Lundin, P.K. Liaw, Fatigue behavior of a wrought Al0.5CoCrCuFeNi two-phase high-entropy alloy, Acta Materialia 99 (2015) 247–258.
[8] Z. Zhang, M.M. Mao, J. Wang, B. Gludovatz, Z. Zhang, S.X. Mao, E.P. George, Q. Yu, R.O. Ritchie, Nanoscale origins of the damage tolerance of the high-entropy alloy CrMnFeCoNi, Nat Commun 6 (2015) 10143.
[9] C. Chen, D. Ye, L. Zhang, J. Liu, Effects of tensile/compressive overloads on fatigue crack growth behavior of an extra-low-interstitial titanium alloy, International Journal of Mechanical Sciences 118 (2016) 55–66.
[10] E.W. Huang, P.K. Liaw, High-temperature materials for structural applications: New perspectives on high-entropy alloys, bulk metallic glasses, and nanomaterials, MRS Bulletin 44 (11) (2019) 847–853.
[11] V. Chaudhary, V. Soni, B. Gwalani, R.V. Ramanujan, R. Banerjee, Influence of non-magnetic Cu on enhancing the low temperature magnetic properties and Curie temperature of FeCoNiCrCu(x) high entropy alloys, Scripta Materialia 182 (2020) 99–103.
[12] O. Senkov, S. Gorsse, D.B. Miracle, High temperature strength of refractory complex concentrated alloys, Acta Materialia 175 (2019) 394–405.
[13] B.S. Murty, J.-W. Yeh, S. Ranganathan, P. Bhattacharjee, High-entropy alloys, Elsevier, 2019.
[14] E.-W. Huang, G.-Y. Hung, S.Y. Lee, J. Jain, K.-P. Chang, J.J. Chou, W.-C. Yang, P.K. Liaw, Mechanical and Magnetic Properties of the High-Entropy Alloys for Combinatorial Approaches, Crystals 10 (3) (2020) 200.
[15] D.B. Miracle, O.N. Senkov, A critical review of high entropy alloys and related concepts, Acta Materialia 122 (2017) 448–511.
[16] E.W. Huang, B. Clausen, Y. Wang, H. Choo, P.K. Liaw, M.L. Benson, L.M. Pike, D.L. Klarstrom, A neutron-diffraction study of the low-cycle fatigue behavior of HASTELLOY® C-22HSTM alloy, International Journal of Fatigue 29 (9) (2007) 1812–1819.
[17] S. Seo, E.W. Huang, W. Woo, S.Y. Lee, Neutron diffraction residual stress analysis during fatigue crack growth retardation of stainless steel, International Journal of Fatigue 104 (2017) 408–415.
[18] S.Y Lee, E.W. Huang, W. Woo, C. Yoon, H. Chae, S.-G. Yoon, Dynamic Strain Evolution around a Crack Tip under Steady- and Overloaded-Fatigue Conditions, Metals 5 (4) (2015) 2109–2118.
[19] S.Y. Lee, Y. Sun, K. An, H. Choo, C.R. Hubbard, P.K. Liaw, Evolution of residual-strain distribution through an overload-induced retardation period during fatigue-crack growth, Journal of Applied Physics 107 (2) (2010) 023517.
[20] R.L. Carlson, G.A. Kardomateas, P.R. Bates, The effects of overloads in fatigue crack growth, International Journal of Fatigue 13 (6) (1991) 453–460.
[21] B. Gludovatz, E.P. George, R.O. Ritchie, Processing, Microstructure and Mechanical Properties of the CrMnFeCoNi High-Entropy Alloy, JOM 67 (10) (2015) 2262–2270.
[22] F. Otto, A. Dlouhý, C. Somsen, H. Bei, G. Eggeler, E.P. George, The influences of temperature and microstructure on the tensile properties of a CoCrFeMnNi high-entropy alloy, Acta Materialia 61 (15) (2013) 5743–5755.
[23] N. Stepanov, M. Tikhonovsky, N. Yurchenko, D. Zyabkin, M. Klimova, S. Zherebtsov, A. Efimov, G. Salishchev, Effect of cryo-deformation on structure and properties of CoCrFeNiMn high-entropy alloy, Intermetallics 59 (2015) 8–17.
[24] K. Suzuki, M. Koyama, S. Hamada, K. Tsuzaki, H. Noguchi, Planar slip-driven fatigue crack initiation and propagation in an equiatomic CrMnFeCoNi high--entropy alloy, International Journal of Fatigue 133 (2020) 105418.
[25] K.V.S. Thurston, B. Gludovatz, A. Hohenwarter, G. Laplanche, E.P. George, R.O. Ritchie, Effect of temperature on the fatigue-crack growth behavior of the high-entropy alloy CrMnFeCoNi, Intermetallics 88 (2017) 65–72.
[26] K.V.S. Thurston, B. Gludovatz, Q. Yu, G. Laplanche, E.P. George, R.O. Ritchie, Temperature and load-ratio dependent fatigue-crack growth in the CrMnFeCoNi high-entropy alloy, Journal of Alloys and Compounds 794 (2019) 525–533.
[27] J. Rackwitz, Q. Yu, Y. Yang, G. Laplanche, E.P. George, A.M. Minor, R.O. Ritchie, Effects of Cryogenic Temperature and Grain Size on Fatigue-Crack Propagation in the Medium-Entropy CrCoNi Alloy, Acta Materialia (2020).
[28] ASTM Standard E647-99: Standard Test Method for Measurement of Fa- tigue Crack Growth Rates, ASME J. Appl. Mech. 03.01 (2000) 591.
[29] E.W. Huang, H.-S. Chou, K.N. Tu, W.-S. Hung, T.-N. Lam, C.-W. Tsai, C.-Y. Chiang, B.-H. Lin, A.-C. Yeh, S.-H. Chang, Y.-J. Chang, J.-J. Yang, X.-Y. Li, C.-S. Ku, K. An, Y.-W. Chang, Y.-L. Jao, Element Effects on High-Entropy Alloy Vacancy and Heterogeneous Lattice Distortion Subjected to Quasi-equilibrium Heating, Scientific Reports 9 (1) (2019) 14788.
[30] E.W. Huang, C.-M. Lin, J.-Y. Juang, Y.-J. Chang, Y.-W. Chang, C.-S. Wu, C.-W. Tsai, A.-C. Yeh, S.R. Shieh, C.-P. Wang, Y.-C. Chuang, Y.-F. Liao, D. Zhang, T. Huang, T.-N. Lam, Y.-H. Chen, Deviatoric deformation kinetics in high entropy alloy under hydrostatic compression, Journal of Alloys and Compounds 792 (2019) 116–121.
[31] E.W. Huang, C.-M. Lin, J. Jain, S.R. Shieh, C.-P. Wang, Y.-C. Chuang, Y.-F. Liao, D.-Z. Zhang, T. Huang, T.-N. Lam, W. Woo, S.Y. Lee, Irreversible phase transformation in a CoCrFeMnNi high entropy alloy under hydrostatic compression, Materials Today Communications 14 (2018) 10–14.
[32] E.W. Huang, D. Yu, J.-W. Yeh, C. Lee, K. An, S.-Y. Tu, A study of lattice elasticity from low entropy metals to medium and high entropy alloys, Scripta Materialia 101 (2015) 32–35.
[33] P.K. Liaw, A. Saxena, V.P. Swaminathan, T.T. Shih, Effects of load ratio and temperature on the near-threshold fatigue crack propagation behavior in a CrMoV steel, Metall. Trans. A 14 (1983) 1631.
[34] W.A. Logsdon, P.K. Liaw, Tensile, fracture toughness and fatigue crack growth rate properties of silicon carbide whisker and particulate reinforced aluminum metal matrix composites, Eng. Fract. Mech. 24 (1986) 737.
[35] P.J. Withers, Mapping residual and internal stress in materials by neutron diffraction, Comptes Rendus Physique 8 (7-8) (2007) 806–820.
[36] E.W. Huang, S.Y. Lee, W. Woo, K.-W. Lee, Three-Orthogonal-Direction Stress Mapping around a Fatigue-Crack Tip Using Neutron Diffraction, Metallurgical and Materials Transactions A 43 (8) (2012) 2785–2791.
[37] L. Velterop, R. Delhez, T.H.D Keijser, E.J. Mittemeijer, D. Reefman, X-ray diffraction analysis of stacking and twin faults in f.c.c. metals, J. Appl. Cryst. 33 (2000) 296–306.
[38] G. Laplanche, P. Gadaud, O. Horst, F. Otto, G. Eggeler, E.P. George, Temperature dependencies of the elastic moduli and thermal expansion coefficient of an equiatomic, single-phase CoCrFeMnNi high-entropy alloy, Journal of Alloys and Compounds 623 (2015) 348–353.
[39] R.B. Von Dreele, A.C. Larson, in: General Structure Analysis System (GSAS), Los Alamos Natl. Lab. Rep. LAUR, 2004, p. 86.
[40] T. Ungár, J. Gubicza, G. Ribárik, MWP-fit a program for multiple whole-profile fitting of diffraction peak profiles by ab initio theoretical functions, J. Appl. Crystallogr. 34 (2001) 669–676.
[41] T. Ungár, Microstructural parameters from X-ray diffraction peak broadening, Scripta Materialia 51 (8) (2004) 777–781.
[42] L. Balogh, G. Ribárik, T. Ungár, Stacking faults and twin boundaries in fcc crystals determined by x-ray diffraction profile analysis, Journal of Applied Physics 100 (2) (2006) 023512.
[43] B. Wang, H. He, M. Naeem, S. Lan, S. Harjo, T. Kawasaki, Y. Nie, H.W. Kui, T. Ungár, D. Ma, A.D. Stoica, Q. Li, Y. Ke, C.T. Liu, X.-L. Wang, Deformation of CoCrFeNi high entropy alloy at large strain, Scripta Materialia 155 (2018) 54–57.
[44] E.W. Huang, R.I. Barabash, B. Clausen, Y.-L. Liu, J.-J. Kai, G.E. Ice, K.P. Woods, P.K. Liaw, Fatigue-induced reversible/irreversible structural-transformations in a Ni-based superalloy, International Journal of Plasticity 26 (8) (2010) 1124–1137.

[45] T.-N. Lam, Y.-S. Chou, Y.-J. Chang, T.-R. Sui, A.-C. Yeh, S. Harjo, S.Y. Lee, J. Jain, B.-H. Lai, E.W. Huang, Comparing Cyclic Tension-Compression Effects on CoCrFeMnNi High-Entropy Alloy and Ni-Based Superalloy, Crystals 9 (8) (2019) 420.
[46] E.W. Huang, C.K. Chang, P.K. Liaw, T.R. Suei, Fatigue induced deformation and thermodynamics evolution in a nano particle strengthened nickel base superalloy, Fatigue & Fracture of Engineering Materials & Structures 39 (6) (2016) 675–685.
[47] T.-N. Lam, C.-W. Tsai, B.-K. Chen, B.-H. Lai, H.-C. Liu, T. Kawasaki, S. Harjo, B.-H. Lin, E.W. Huang, Element Effects of Mn and Ge on the Tuning of Mechanical Properties of High-Entropy Alloys, Metallurgical and Materials Transactions A 51 (2020) 5023–5028.
[48] C.V. Sushma, D.P.R. Reddy, P. R. Lakshmi, Investigation Of Fracture Parameters Of Compact Tension Specimen By FEA, International Journal of Engineering Research & Technology (IJERT) 2 (6) (2013) 1587–1591.
[49] Y. Gori, R.P. Verma, Estimation of Plastic Zone at Crack Tip Under Fatigue Loading of AA6061-T6 Aluminum Alloy by Finite Element Analysis Using ANSYS, In: Prasad A., Gupta S., Tyagi R. (eds) Advances in Engineering Design. Lecture Notes in Mechanical Engineering, Springer, Singapore., 2019, pp. 595–606.
[50] X. Ji, F. Zhu, Finite element simulation of elastoplastic field near crack tips and results for a central cracked plate of LE-LHP material under tension, Acta Mechanica Sinica 35 (4) (2019) 828–838.
[51] S.-K. Kim, C.-S. Lee, J.-H. Kim, M.-H. Kim, B.-J. Noh, T. Matsumoto, J.-M. Lee, Estimation of Fatigue Crack Growth Rate for 7% Nickel Steel under Room and Cryogenic Temperatures Using Damage-Coupled Finite Element Analysis, Metals 5 (2) (2015) 603–627.
[52] G.R. Irwin, Analysis of stresses and strains near the end of a crack transversing a plate, ASME J. Appl. Mech. 24 (1957) 361.
[53] K. Sadananda, A.K. Vasudevan, R.L. Holtz, E.U. Lee, Analysis of overload effects and related phenomena, International Journal of Fatigue 21 (1999) S233–S246.
[54] R. Barabash, Y. Gao, Y. Sun, S.Y. Lee, H. Choo, P.K. Liaw, D.W. Brown, G.E. Ice, Neutron and X-ray diffraction studies and cohesive interface model of the fatigue crack deformation behavior, Philosophical Magazine Letters 88 (8) (2008) 553–565.
[55] S.M. Ohr, S. Kobayashi, In situ observations of the formation of plastic zone ahead of a crack tip in copper, Scripta Metallurgica 15 (1981) 343–348.
[56] S.-W. Kim, J.H. Kim, In-situ observations of deformation twins and crack propagation in a CoCrFeNiMn high-entropy alloy, Materials Science and Engineering: A 718 (2018) 321–325.
[57] A.J. Zaddach, C. Niu, C.C. Koch, D.L. Irving, Mechanical Properties and Stacking Fault Energies of NiFeCrCoMn High-Entropy Alloy, JOM 65 (12) (2013) 1780–1789.
[58] Y.H. Zhang, Y. Zhuang, A. Hu, J.J. Kai, C.T. Liu, The Origin of Negative Stacking Fault Energies and Nano-twin Formation in Face-Centered Cubic High Entropy Alloys, Scripta Materialia 130 (2017) 96–99.
[59] C. Niu, C.R. LaRosa, J. Miao, M.J. Mills, M. Ghazisaeidi, Magnetically-driven phase transformation strengthening in high entropy alloys, Nature Communications 9 (1) (2018) 1363.
[60] Y.T. Zhu, X.Z. Liao, X.L. Wu, J. Narayan, Grain size effect on deformation twinning and detwinning, Journal of Materials Science 48 (13) (2013) 4467–4475.
[61] W. Wu, S.Y. Lee, A.M. Paradowska, Y. Gao, Peter K. Liaw, Twinning-detwinning behavior during fatigue-crack propagation in a wrought magnesium alloy AZ31B, Materials Science and Engineering A 556 (2012) 278–286.
[62] N.S. Prasad, N. Naveen Kumar, R. Narasimhan, S. Suwas, Fracture behavior of magnesium alloys – Role of tensile twinning, Acta Materialia 94 (2015) 281–293.
[63] G. Laplanche, A. Kostka, O.M. Horst, G. Eggeler, E.P. George, Microstructure evolution and critical stress for twinning in the CrMnFeCoNi high-entropy alloy, Acta Materialia 118 (2016) 152–163.
[64] L.W. Tsay, Y.C. Liu, M.C. Young, D.-Y. Lin, Fatigue crack growth of AISI 304 stainless steel weldsin air and hydrogen, Materials Science and Engineering A 374 (2004) 204–210.
[65] A.-L. Gloanec, G. Hénaff, D. Bertheau, P. Belaygue, M. Grange, Fatigue crack growth behaviour of a gamma-titanium-aluminide alloy prepared by castingand powder metallurgy, Scripta Materialia 49 (2003) 825–830.
[66] I.V. Singh, B.K Mishra, S. Bhattacharya, R.U. Patil, The numerical simulation of fatigue crack growth using extended finiteelement method, International Journal of Fatigue 36 (2012) 109–119.
[67] S.G. Song, G.T. Gray, Influence of temperature and strain rate on slip and twinning behavior of zr, Metallurgical and Materials Transactions A volume 26 (1995) 2665–2675.